*Geophys. J. Int.* (2008) **174,** 808–814 doi: 10.1111/j.1365-246X.2008.03875.x



# Synthetic logs of multipole sources in boreholes based on the Kelvin–Voigt stress–strain relation

José M. Carcione and Flavio Poletto

*Istituto Nazionale di Oceanografia e di Geofisica Sperimentale (OGS), Borgo Grotta Gigante* 42c, 34010 *Sgonico, Trieste, Italy.*
*E-mail: jcarcione@ogs.trieste.it*

Accepted 2008 May 28. Received 2008 May 28; in original form 2008 March 6

## SUMMARY

We design a numerical algorithm for wave simulation in a borehole due to multipole sources. The stress–strain relation of the formation is based on the Kelvin–Voigt mechanical model to describe the attenuation. The modelling, which requires two anelastic parameters and twice the spatial derivatives of the lossless case, simulates 3-D waves in an axisymmetric medium by using the Fourier and Chebyshev methods to compute the spatial derivatives along the vertical and horizontal directions, respectively. Instabilities of the Chebyshev differential operator due to the implementation of the fluid–solid boundary conditions are solved with a characteristic approach, where the characteristic variables are evaluated at the source central frequency. The algorithm uses two meshes to model the fluid and the solid. The presence of the logging tool is modelled by imposing rigid boundary conditions at the inner surface of the fluid mesh. Examples illustrating the propagation of waves are presented, namely, by using monopoles, dipoles and a quadrupoles as sources in hard and soft formations. Moreover, the presence of casing and layers is considered. The modelling correctly simulates the features—traveltime and attenuation—of the wave modes observed in sonic logs, namely, the *P* and *S* body waves, the Stoneley wave, and the dispersive *S* waves in the case of multipole sources.

**Key words:** Numerical solutions; Fourier analysis; Downhole methods; Geomechanics; Seismic attenuation; Wave propagation.

## 1 INTRODUCTION

Guided waves through a borehole can be used to control the drilling conditions and to obtain the petro-physical properties of the surrounding formation (e.g. Carcione & Poletto 2000). In particular, full-waveform sonic-log tools measure the *P*- and *S*-wave velocities and attenuation factors (Paillet & Cheng 1991). These properties provide information about the rock type, the porosity, the fluid saturation, the presence of fractures and the *in situ* stress conditions. The laboratory experiments conducted by Chen (1982) provide a clear picture of the different wave modes. If the *P*- and *S*-wave velocities of the formation are greater than the *P*-wave (sound) velocity of the borehole fluid (hard formation), the wave train consists of refracted *P*- and *S*-waves, guided waves (pseudo-Rayleigh waves) and a Stoneley wave. The first two are body waves, the guided modes are highly dispersive and have a velocity ranging from the *S*-wave velocity to a fraction of the fluid sound velocity. The Stoneley wave has a velocity smaller than the fluid velocity, a high amplitude and is not very dispersive.

When the *S*-wave velocity is less than the fluid sound velocity (soft formation), there is no refracted *S* wave, and leaky *P* waves may interfere with the refracted *P* wave. A solution to separate them is to use dipole sources (Tichelaar & van Luik 1995). Modal *S*-wave trains can be generated with multipole sources. The radiation intensity of multipole sources depends on the azimuthal angle $\theta$ about the borehole axis as $\exp(in\theta)$, where $i = \sqrt{-1}$ and $n$ is the multipole order. For instance, $n = 0$ is a monopole, $n = 1$ is a dipole and $n = 2$ is a quadrupole. Multipole sources are useful to excite certain wave modes (Winbow 1985, 1991; Chen 1988, 1989). For instance, high-order sources are effective to generate *S* waves. The experiments conducted by Chen (1989) using quadrupole sources are very illustrative. While monopole sources in limestone (hard formation) generate *P* waves and low-frequency Stoneley waves, quadrupole waveforms do not show these waves. Also, modal (guided) waves can and cannot be excited depending if the source frequency is higher or lower than the entry frequencies of the modes. While monopole waveforms in plastic (soft formation) generate clear *P* and Stoneley waves, quadrupole sources generate *P* and modal *S* waves above the entry frequency and only modal *S* waves below the entry frequency. Dipole sources generate flexural modes and quadrupole sources excite screw modes (Kumar & Ram 1969; Kurkjian & Chang 1986).

Numerical modelling in the frequency–wavenumber domain, known as the real axis integration (RAI), the branch-cut integration (BCI) or the discrete wavenumber (DW) method, is fast and effective but restricted to uniform properties in the axial and azimuthal directions (White & Zechman 1968; Kurkjian & Chang 1986). Randall *et al.* (1991) first modelled multipole sources in

azimuthally uniform media using the velocity–stress formulation and a staggered finite-difference grid. Mittet & Renlie (1996) introduce attenuation and anisotropy and solve the same problem using high-order finite differences to reduce the computational cost. A fully 3-D finite-difference code has been developed by Chen *et al.* (1998), who simulate wave propagation in the presence of the sonic well-logging tool.

The algorithm proposed here simulates synthetic seismograms generated by multipole borehole sources in an axisymmetric medium described by the Kelvin–Voigt constitutive equation. A similar stress–strain relation, in Cartesian coordinates, has been proposed to propagate 3-D waves in the presence of the Earth's surface (Carcione *et al.* 2004). The novel features of the present method is the use of cylindrical coordinates, pseudospectral differentiation, domain decomposition to model the fluid–solid interface, multipole sources, and the description of dissipation without additional field variables. Most of the time-domain modelling algorithms require the use of additional (memory) variables to model anelasticity. Generally, this approach is based on the use of the generalized Zener model (Carcione 2007) or the generalized Maxwell model (Emmerich & Korn 1987; Mittet & Renlie 1996). Use of memory variables can be expensive in three dimensions, since the Zener model requires six variables for each relaxation mechanism (Carcione 2007). The Kelvin–Voigt mechanical model is not based on memory variables (Ben-Menahem & Singh 1981; Carcione 2007), and its implementation requires the calculations of additional spatial derivatives and the use of two anelastic parameters compared to four parameters when using the Zener model.

The present algorithm simulates 3-D axisymmetric waves in a 2-D multidomain, where the radial spatial derivatives are computed with the Chebyshev method and the vertical spatial derivatives are computed with the Fourier method (e.g. Carcione 2007). Both differentiations are implemented with the fast Fourier transform. The algorithm uses two meshes in cylindrical coordinates, corresponding to the fluid and solid media. The meshes are combined by decomposing the wave field into incoming and outgoing wave modes at the interface between the media, and modifying these modes on the basis of the fluid–solid boundary conditions (Carcione 1991, 1996). The inner surface, corresponding to the tool–mud interface, satisfies rigid conditions.

## 2 EQUATIONS OF MOMENTUM CONSERVATION

The axisymmetric 3-D equations of momentum conservation for the solid in cylindrical coordinates can be written as (Fung 1965; Mittet & Renlie 1996)

$$\dot{v}_r = \Pi_r, \quad \dot{v}_\theta = \Pi_\theta, \dot{v}_z = \Pi_z, \tag{1}$$

where

$$\rho\Pi_r = \frac{1}{r}\left[\frac{\partial}{\partial r}(r\sigma_{rr}) + n\sigma_{r\theta} - \sigma_{\theta\theta}\right] + \frac{\partial\sigma_{rz}}{\partial z} + f_r, \tag{2}$$

$$\rho\Pi_\theta = \frac{1}{r}(2\sigma_{r\theta} - n\sigma_{\theta\theta}) + \frac{\partial\sigma_{r\theta}}{\partial r} + \frac{\partial\sigma_{\theta z}}{\partial z} + f_\theta, \tag{3}$$

$$\rho\Pi_z = \frac{1}{r}\left[n\sigma_{\theta z} + \frac{\partial}{\partial r}(r\sigma_{rz})\right] + \frac{\partial\sigma_{zz}}{\partial z} + f_z, \tag{4}$$

where $r$, $\theta$ and $z$ are the spatial variables, $n$ is the order of the multipole source, $\rho$ is the density, the $\sigma$'s are stress components, the $v$'s are particle velocities and the $f$'s are body forces per unit volume. A dot above a variable denotes time differentiation.

The corresponding equations for the fluid are

$$\rho\dot{v}_r = -\frac{\partial p}{\partial r} + f_r, \quad \rho\dot{v}_\theta = \frac{n}{r}p + f_\theta, \quad \rho\dot{v}_z = -\frac{\partial p}{\partial z} + f_z, \tag{5}$$

where $p = -\sigma_{rr}$ is the fluid pressure.

These and the stress–strain equations below result from assuming that the quantities $v_\theta, \sigma_{r\theta}, \sigma_{\theta z}, f_\theta, f_{\theta z}$ and $f_{r\theta}$ are proportional to $\sin n\theta$ while the other variables are proportional to $\cos n\theta$ (Randall *et al.* 1991). A monopole corresponds to $n = 0$, a dipole to $n = 1$, a quadrupole to $n = 2$, etc.

## 3 STRESS–STRAIN RELATIONS

The 3-D stress–strain relations for the solid are given by

$$\dot{\sigma}_{rr} = \lambda\vartheta + 2\mu\frac{\partial v_r}{\partial r} + \lambda'\dot{\vartheta} + 2\mu'\frac{\partial\dot{v}_r}{\partial r} + f_{rr}, \tag{6}$$

$$\dot{\sigma}_{\theta\theta} = \lambda\vartheta + 2\mu\left(\frac{v_r}{r} + \frac{n}{r}v_\theta\right) + \lambda'\dot{\vartheta} + 2\mu'\left(\frac{\dot{v}_r}{r} + \frac{n}{r}\dot{v}_\theta\right) + f_{\theta\theta}, \tag{7}$$

$$\dot{\sigma}_{zz} = \lambda\vartheta + 2\mu\frac{\partial v_z}{\partial z} + \lambda'\dot{\vartheta} + 2\mu'\frac{\partial\dot{v}_z}{\partial z} + f_{zz}, \tag{8}$$

$$\dot{\sigma}_{\theta z} = \mu\left(\frac{\partial v_\theta}{\partial z} - \frac{n}{r}v_z\right) + \mu'\left(\frac{\partial\dot{v}_\theta}{\partial z} - \frac{n}{r}\dot{v}_z\right) + f_{\theta z}, \tag{9}$$

$$\dot{\sigma}_{rz} = \mu\left(\frac{\partial v_r}{\partial z} + \frac{\partial v_z}{\partial r}\right) + \mu'\left(\frac{\partial\dot{v}_r}{\partial z} + \frac{\partial\dot{v}_z}{\partial r}\right) + f_{rz}, \tag{10}$$

$$\dot{\sigma}_{r\theta} = \mu\left(\frac{\partial v_\theta}{\partial r} - \frac{v_\theta}{r} - \frac{n}{r}v_r\right) + \mu'\left(\frac{\partial\dot{v}_\theta}{\partial r} - \frac{\dot{v}_\theta}{r} - \frac{n}{r}\dot{v}_r\right) + f_{r\theta}, \tag{11}$$

$$\vartheta = \frac{\partial v_r}{\partial r} + \frac{\partial v_z}{\partial z} + \frac{v_r}{r} + \frac{n}{r}v_\theta, \tag{12}$$

where $\lambda$ and $\mu$ are the Lamé constants, $\lambda'$ and $\mu'$ are the Kelvin–Voigt anelastic parameters (Carcione *et al.* 2004), $\vartheta$ is the dilatation, and $f_{ab}$ are stress forces.

Substituting eqs (2)–(4) into (6)–(11) yields

$$\dot{\sigma}_{rr} = \lambda\vartheta + 2\mu\frac{\partial v_r}{\partial r} + \lambda'\psi + 2\mu'\frac{\partial\Pi_r}{\partial r} + f_{rr}, \tag{13}$$

$$\dot{\sigma}_{\theta\theta} = \lambda\vartheta + 2\mu\left(\frac{v_r}{r} + \frac{n}{r}v_\theta\right) + \lambda'\psi + 2\mu'\left(\frac{\Pi_r}{r} + \frac{n}{r}\Pi_\theta\right) + f_{\theta\theta}, \tag{14}$$

$$\dot{\sigma}_{zz} = \lambda\vartheta + 2\mu\frac{\partial v_z}{\partial z} + \lambda'\psi + 2\mu'\frac{\partial\Pi_z}{\partial z} + f_{zz}, \tag{15}$$

$$\dot{\sigma}_{\theta z} = \mu\left(\frac{\partial v_\theta}{\partial z} - \frac{n}{r}v_z\right) + \mu'\left(\frac{\partial\Pi_\theta}{\partial z} - \frac{n}{r}\Pi_z\right) + f_{\theta z}, \tag{16}$$

$$\dot{\sigma}_{rz} = \mu\left(\frac{\partial v_r}{\partial z} + \frac{\partial v_z}{\partial r}\right) + \mu'\left(\frac{\partial\Pi_r}{\partial z} + \frac{\partial\Pi_z}{\partial r}\right) + f_{rz}, \tag{17}$$

$$\dot{\sigma}_{r\theta} = \mu\left(\frac{\partial v_\theta}{\partial r} - \frac{v_\theta}{r} - \frac{n}{r}v_r\right) + \mu'\left(\frac{\partial\Pi_\theta}{\partial r} - \frac{\Pi_\theta}{r} - \frac{n}{r}\Pi_r\right) + f_{r\theta}, \tag{18}$$

$$\psi = \dot{\vartheta} = \frac{\partial \Pi_r}{\partial r} + \frac{\partial \Pi_z}{\partial z} + \frac{\Pi_r}{r} + \frac{n}{r}\Pi_\theta. \tag{19}$$

The Kelvin–Voigt model requires less storage and field variables to describe attenuation compared to the Zener and Maxwell models. For instance, consider that the model is discretized in two meshes with $n_r \times n_z$ grid points each. The number of unknown field variables using the velocity–stress formulation is nine (three particle-velocity components and six stress components). The Zener model requires six additional arrays to describe attenuation, and six arrays for the material properties (two elastic constants and four relaxation times). Then, the total RAM storage occupied by the Zener model is $42 \times n_r \times n_z$. On the other hand, the Kelvin–Voigt model requires nine arrays for the field variables and four arrays for the material properties, implying a storage of $26 \times n_r \times n_z$. Therefore, the saving in storage is more than 40 per cent. The drawback is that the Kelvin–Voigt model requires the calculation of nine additional spatial derivatives at each time step, compared to the Zener model. However, the saving in computer storage can be significant when modelling 3-D wave propagation.

The corresponding constitutive equation for the fluid is

$$-\dot{p} = \dot{\sigma}_{rr} = \lambda\vartheta + f_{rr}, \tag{20}$$

where we have assumed no intrinsic losses.

In order to simulate multipoles sources, we assume the following function

$$f_{ab} = \delta_{ab}\delta(r - r_s)\delta(z - z_s)f(t),\ a = r,\ \theta, z. \tag{21}$$

where $f(t)$ is the time history of the source.

## 4 FREQUENCY-DOMAIN ANALYSIS

The phase velocity and quality factor of the solid are given by (Carcione *et al.* 2004; Carcione 2007)

$$v = \left[\mathrm{Re}\left(\frac{1}{v_c}\right)\right]^{-1} \tag{22}$$

and

$$Q = \frac{\mathrm{Re}\left(v_c^2\right)}{\mathrm{Im}\left(v_c^2\right)}, \tag{23}$$

where $v_c$ is either the $P$-wave complex velocity or the $S$-wave complex velocity. They are given by

$$v_{cP} = \sqrt{\frac{\Lambda + 2\Sigma}{\rho}} \quad \text{and} \quad v_{cS} = \sqrt{\frac{\Sigma}{\rho}}, \tag{24}$$

respectively, where

$$\Lambda = \lambda + i\omega\lambda', \quad \text{and} \quad \Sigma = \mu + i\omega\mu', \tag{25}$$

$\omega$ is the angular frequency, and Re and Im take real and imaginary parts.

The phase velocities of the $P$ and $S$ waves tend to $\sqrt{E/\rho}$ and $\sqrt{\mu/\rho}$ for $\omega \to 0$, and to $\infty$ for $\omega \to \infty$, where $E = \lambda + 2\,\mu$. The $P$- and $S$-wave quality factor are simply

$$Q_P = \frac{E}{\omega E'}, \quad \text{and} \quad Q_S = \frac{\mu}{\omega\mu'}, \tag{26}$$

where $E' = \lambda' + 2\mu'$. The attenuation factor is given by (Carcione 2007)

$$\alpha = \frac{\omega}{v}[\sqrt{1 + Q^2} - Q]. \tag{27}$$

For low-loss media ($Q \gg 1$), eq. (27) becomes

$$\alpha_P = \frac{\omega^2 E'}{2E v_P} \quad \text{and} \quad \alpha_S = \frac{\omega^2 \mu'}{2\mu v_S}, \tag{28}$$

where eqs (26) have been used. Then, the attenuation factor is approximately proportional to the square of the frequency if the variation of the phase velocity is small over the range of frequencies of the signal.

The anelastic parameters can be obtained from the quality factors at a given frequency, say, the central frequency of the source, $\omega_0$. We obtain

$$\lambda' = \frac{1}{\omega_0}\left(\frac{E}{Q_{P0}} - \frac{2\mu}{Q_{S0}}\right) \quad \text{and} \quad \mu' = \frac{\mu}{\omega_0 Q_{S0}}, \tag{29}$$

where $Q_{P0}$ and $Q_{S0}$ are the quality factors at $\omega = \omega_0$, and $E$ and $\mu$ are the moduli at $\omega = 0$.

The moduli can be obtained from the $P$- and $S$-wave phase velocities at $\omega = \omega_0$, $v_{P0}$ and $v_{S0}$, respectively. Using eqs (25), (22), (24) and (26) gives

$$E = \rho v_{P0}^2 g(Q_{P0}) \quad \text{and} \quad \mu = \rho v_{S0}^2 g(Q_{S0}), \tag{30}$$

where

$$g(a) = \frac{1}{2}(1 + a^{-2})^{-1/2}\left[1 + (1 + a^{-2})^{-1/2}\right]. \tag{31}$$

Note that $g(a) \to 1$ when $a \to \infty$. Hence, the input properties to the modelling program are $\rho$, $v_{P0}$, $v_{S0}$, $Q_{P0}$ and $Q_{S0}$.

## 5 BOUNDARY CONDITIONS AND DOMAIN-DECOMPOSITION

The solution on each grid is obtained by using a fourth-order Runge–Kutta method as time stepping algorithm, the Chebyshev differential operator (Carcione 1996, 2007) to compute the spatial derivatives along the radial direction and the Fourier differential operator (Carcione 2007) along the vertical direction. The Gauss–Lobatto collocation points are defined as $r_i = -\cos[\pi(i - 1)/(n_r - 1)]$, $i = 1, \ldots, n_r$, where $n_r$ is the number of radial grid points. An analysis of the stability and accuracy of the algorithm due to the use of the Kelvin–Voigt stress–strain relation and the Runge–Kutta method has been performed in Carcione *et al.* (2004), where the numerical approximation of the phase velocity and quality factor were obtained. These quantities depend on the time step, which is determined to satisfy the accuracy requirements by comparison to the exact phase velocity (7) and quality factor (8).

To combine the grids, the wave field is decomposed into incoming and outgoing wave modes at the interface between the media (Carcione 1991, 2007). The algorithm can be outlined as follows. Let us consider the solid material. Eqs (1) and (13)–(18) can be expressed in matrix notation as $\dot{\mathbf{v}} = \mathbf{H}\mathbf{v} \equiv \mathbf{A}\partial_r\mathbf{v} + \mathbf{B}\partial_z\mathbf{v}$, where $\mathbf{H}$ is the differential–operator matrix and $\mathbf{v}$ is the unknown wave field (particle velocities and stresses), and we have omitted the sources for simplicity. The Runge–Kutta method computes the operation $\mathbf{H}\mathbf{v} \equiv (\mathbf{v})^{\mathrm{old}}$. The vector $(\mathbf{v})^{\mathrm{old}}$ is then updated to give a new vector $(\mathbf{v})^{\mathrm{new}}$ that takes into account the boundary conditions. Consider a boundary parallel to the $z$-axis (e.g. the borehole wall). Compute the eigenvalues of matrix $\mathbf{A}$. Compute the right eigenvectors of matrix $\mathbf{A}$, such that they are the columns of matrix $\mathbf{R}$, where $\mathbf{A} = \mathbf{R}\mathbf{\Lambda}\mathbf{R}^{-1}$, with $\mathbf{\Lambda}$ the diagonal matrix of the eigenvalues. The characteristics vector is $\mathbf{c} = \mathbf{R}^{-1}\,\mathbf{v}$, and the above equation of motion corresponding to the $r$-direction becomes $\dot{\mathbf{c}} = \mathbf{\Lambda}\partial_r\mathbf{c}$, where the incoming and outgoing waves are decoupled. Similarly, a characteristics vector can

be obtained for the fluid medium: $\mathbf{c}' = \mathbf{R}'^{-1}\,\mathbf{v}'$. The outgoing characteristics satisfy $(\mathbf{c})^{\rm new} = (\mathbf{c})^{\rm old}$ and $(\mathbf{c}')^{\rm new} = (\mathbf{c}')^{\rm old}$. These equations complemented with the boundary conditions yield the following equations for updating the field variables at the grid points defining the interface between media 1 (the fluid) and 2 (the solid):

$$v_r^{(\rm new)}(1,2) = \frac{1}{Z_P(1)+Z_P(2)}\Big[Z_P(1)v_r^{(\rm old)}(1) + Z_P(2)v_r^{(\rm old)}(2) \pm \sigma_{rr}^{(\rm old)}(1) \mp \sigma_{rr}^{(\rm old)}(2)\Big], \tag{32}$$

$$v_\theta^{(\rm new)}(2) = v_\theta^{(\rm old)}(2) \mp \frac{1}{Z_S}\sigma_{r\theta}^{(\rm old)}(2), \tag{33}$$

$$v_z^{(\rm new)}(2) = v_z^{(\rm old)}(2) \mp \frac{1}{Z_S}\sigma_{rz}^{(\rm old)}(2), \tag{34}$$

$$\sigma_{rr}^{(\rm new)}(1,2) = \frac{Z_P(1)Z_P(2)}{Z_P(1)+Z_P(2)}\Big[\pm v_r^{(\rm old)}(1) \mp v_r^{(\rm old)}(2) + \frac{1}{Z_P(1)}\sigma_{rr}^{(\rm old)}(1) + \frac{1}{Z_P(2)}\sigma_{rr}^{(\rm old)}(2)\Big], \tag{35}$$

$$\sigma_{\theta\theta}^{(\rm new)}(2) = \sigma_{\theta\theta}^{(\rm old)}(2) + \frac{\lambda_0}{E_0}\left[\sigma_{rr}^{(\rm new)}(2) - \sigma_{rr}^{(\rm old)}(2)\right], \tag{36}$$

$$\sigma_{zz}^{(\rm new)}(2) = \sigma_{zz}^{(\rm old)}(2) + \frac{\lambda_0}{E_0}\left[\sigma_{rr}^{(\rm new)} - \sigma_{rr}^{(\rm old)}(2)\right], \tag{37}$$

$$\sigma_{r\theta}^{(\rm new)}(2) = \sigma_{rz}^{(\rm new)}(2) = 0, \tag{38}$$

where $Z_P = \rho v_{P0}$, $Z_S = \rho v_{S0}$, $\lambda_0 = \rho(v_{P0}^2 - 2v_{S0}^2)$ and $E_0 = \rho v_{P0}^2$. The upper signs correspond to the fluid–solid boundary and the lower signs to the solid/fluid boundary. We have considered the characteristics at the central frequency of the source. That is, velocities and impedances are taken at $\omega = \omega_0$ (see Section 4).

We choose the inner radius of the inner grid to be equal to the radius of the logging tool. The tool–fluid interface satisfies rigid boundary conditions:

$$v_r^{(\rm new)} = 0, \tag{39}$$

$$\sigma_{rr}^{(\rm new)} = \sigma_{rr}^{(\rm old)} - Z_P v_r^{(\rm old)}. \tag{40}$$

The non-reflecting conditions at the outer boundary of the outer grid are

$$v_r^{(\rm new)} = 0.5\left[v_r^{(\rm old)} + \frac{1}{Z_P}\sigma_{rr}^{(\rm old)}\right], \tag{41}$$

$$v_\theta^{(\rm new)} = 0.5\left[v_\theta^{(\rm old)} + \frac{1}{Z_S}\sigma_{r\theta}^{(\rm old)}\right], \tag{42}$$

$$v_z^{(\rm new)} = 0.5\left[v_z^{(\rm old)} + \frac{1}{Z_S}\sigma_{rz}^{(\rm old)}\right], \tag{43}$$

$$\sigma_{rr}^{(\rm new)} = 0.5[\sigma_{rr}^{(\rm old)} + Z_P v_r^{(\rm old)}], \tag{44}$$

$$\sigma_{r\theta}^{(\rm new)} = 0.5[\sigma_{r\theta}^{(\rm old)} + Z_S v_\theta^{(\rm old)}], \tag{45}$$

$$\sigma_{rz}^{(\rm new)} = 0.5[\sigma_{rz}^{(\rm old)} + Z_S v_z^{(\rm old)}], \tag{46}$$

$$\sigma_{\theta\theta}^{(\rm new)} = \sigma_{\theta\theta}^{(\rm old)} + \frac{\lambda_0}{E_0}\left[\sigma_{rr}^{(\rm new)} - \sigma_{rr}^{(\rm old)}\right], \tag{47}$$

$$\sigma_{zz}^{(\rm new)} = \sigma_{zz}^{(\rm old)} + \frac{\lambda_0}{E_0}\left[\sigma_{rr}^{(\rm new)} - \sigma_{rr}^{(\rm old)}\right]. \tag{48}$$

In addition to the non-reflecting conditions, absorbing strips are used to further attenuate the wave field at the outer radial boundary and top and bottom of the grids (Carcione 1996).

## 6 SIMULATIONS

The geometry of a logging tool embedded in a borehole is shown in Fig. 1, where the tool is the inner cylinder. Then follows the fluid annulus, a solid (the casing in the example) and an unbounded solid (the formation). The bi-mesh is shown in Fig. 2, where the location of the grid points in the radial direction can be appreciated.

First, we consider a homogeneous formation (without casing) and the following data to run the simulation. Fluid: $n_r = 31$, $n_z = 125$, $dz = 0.04$ m, $r_{\rm min} = 5$ cm, $r_{\rm max} = 12.4$ cm, $\rho = 1\,{\rm g\,cm^{-3}}$, $v_{P0} = 1.5\ {\rm km\,s^{-1}}$ (the minimum radial grid spacing is 0.46 mm); Solid: $n_r = 121$, $n_z = 125$, $dz = 0.04$ m, $r_{\rm min} = 12.4$ cm, $r_{\rm max} = 2$ m (the minimum radial grid spacing is 1.5 mm); Hard formation: $\rho = 2.5\,{\rm g\,cm^{-3}}$, $v_{P0} = 4\ {\rm km\,s^{-1}}$, $v_{S0} = 2.3\ {\rm km\,s^{-1}}$, $Q_{P0} = 50$, $Q_{S0} = 40$; Soft formation: $\rho = 1.3\,{\rm g\,cm^{-3}}$, $v_{P0} = 2.5\ {\rm km\,s^{-1}}$, $v_{S0} = 1.17\ {\rm km\,s^{-1}}$, $Q_{P0} = 30$, $Q_{S0} = 20$. The material properties correspond to a reference frequency of $f_0 = 9$ kHz. Fig. 3 shows the $P$-wave phase velocity and dissipation factor ($1/Q_P$) versus frequency, corresponding to the hard formation. The phase velocity and dissipation factor increase with frequency and tend to infinity for infinite frequency. Note that at 9 kHz the quality factor is equal to 50.

The source ($f_{rr}$) and the receivers are located in the fluid at the centre of the grid. The source emits a pulse of peak frequency $f_0 =$ 9 KHz with a duration of approximately 0.25 ms, and the solution is

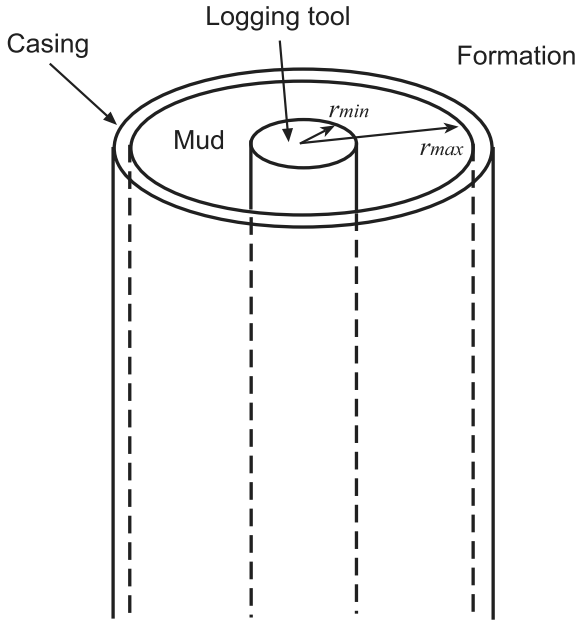


**Figure 1.** Geometry of an idealized logging tool and borehole. The radii correspond to the tool and borehole. The inner surface satisfies rigid boundary conditions to model the fluid–tool interface. An example with casing is shown.

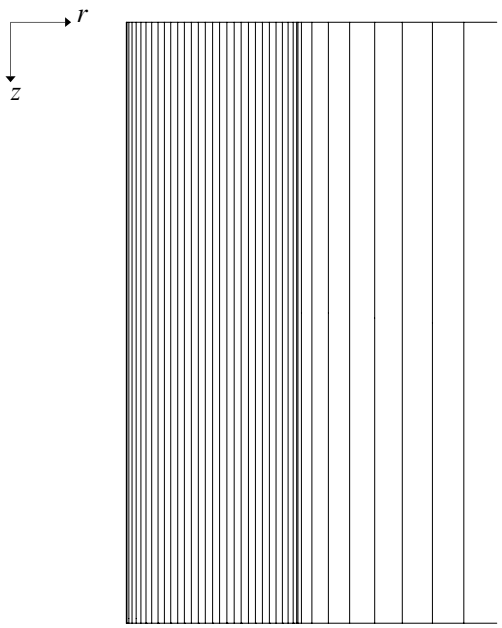


**Figure 2.** Detail of the meshes in the radial direction. Eight points of the formation mesh can be seen at the right side. The left boundary satisfies rigid boundary conditions to model the logging tool.

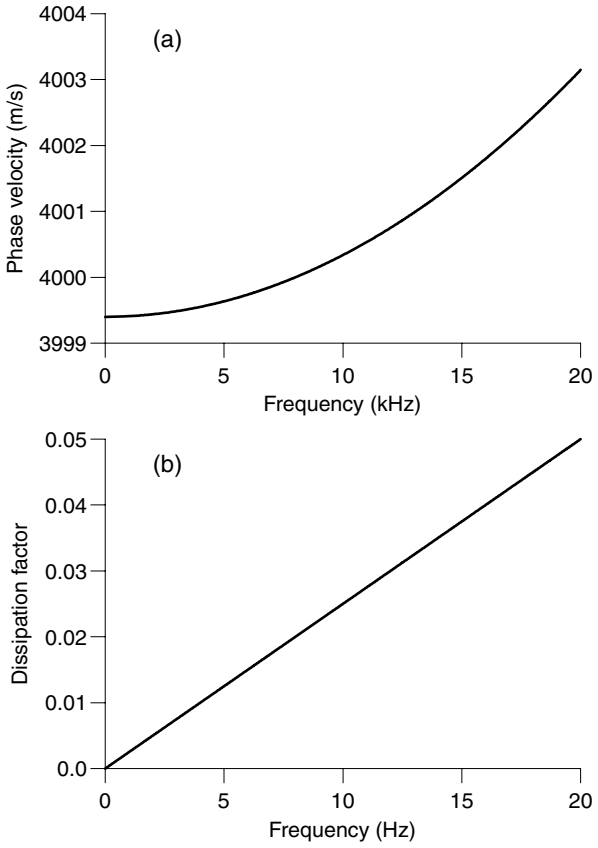


**Figure 3.** *P*-wave phase velocity (a) and dissipation factor (b) ($1/Q_P$) versus frequency. At 9 kHz the velocity is 4 km s$^{-1}$ and the quality factor is 50.

propagated to 2.5 ms with a time step of 0.04 $\mu$s. The source time-history used in the simulations is a Ricker wavelet whose spectrum is a Gaussian centred at the peak frequency. Its expression can be found in Carcione (2007) (eqs 2.233 and 2.234).

The low-frequency limit velocity of the tube wave, also called Stoneley wave, in a lossless medium, is, approximately (White 1965; Norris 1990)

$$v_T = \left\{\rho_f \left[\frac{1}{K_f} + \frac{1}{1-\eta}\left(\frac{1}{\mu_s} + \frac{\eta}{\mu_t}\right)\right]\right\}^{-1/2}, \tag{49}$$

where $K_f$ is the bulk modulus of the fluid, $\rho_f$ is the fluid density, $\mu_s$ is the shear modulus of the formation, $\mu_t$ is the shear modulus of the logging tool, and $\eta$ is the volume fraction of the tool relative to the borehole: $\eta = r_{\rm min}^2/r_{\rm max}^2$. The rigid condition at the tool implies $\mu_t = \infty$. At the reference frequency, we may assume that $K_f = \rho_f v_{P0}^2$ (fluid) and $\mu_s = \rho_s v_{S0}^2$ (formation). We obtain $\eta = 0.16$, $v_T = 1367$ m s$^{-1}$ (hard formation) and $v_T = 946$ m s$^{-1}$ (soft formation).

The velocity of the Stoneley wave without tool in the presence of casing is

$$v_T = \left[\rho_f \left(\frac{1}{K_f} + \frac{1}{N}\right)\right]^{-1/2}, \tag{50}$$

$$N = \frac{2(1-\nu)\mu_s + (\mu - \mu_s)(1-a^2)}{2(1-\nu) - (1-\mu_s/\mu)(1-2\nu)(1-a^2)}, \tag{51}$$

where $a = r_c/r_c'$, with $r_c$ and $r_c'$ the inner and outer radii of the casing, and $\mu$ and $\nu$ the shear modulus and Poisson ratio of the steel casing. This equation has been obtained by Marzetta & Schoenberg (1985) and is a correction of a similar expression obtained by White (1965). Let us assume that $r_c = 0.124$ m, $r_c' = 0.134$ m, and that the casing properties are $\rho = 7.85$ g cm$^{-3}$, $v_{P0} = 5.9$ km s$^{-1}$ and $v_{S0} = 3.19$ km s$^{-1}$. We obtain $v_T = 1357$ m s$^{-1}$ for a soft formation.

Fig. 4 shows the velocity of the Stoneley wave as a function of the shear wave velocity of the formation for different cases. We have assumed $\rho[\text{kg m}^{-3}] = 397\ (v_{S0}\ [\text{m s}^{-1}])^{1/4}$. As can be seen, the presence of casing increases the tube-wave velocity for soft formations. This has a consequence on the visibility of the tube wave, which is masked by the water wave (see Fig. 9 below).

Figs 5 and 6 shows the $\sigma_{rr}$ waveforms due to a monopole source, corresponding to the soft and hard formations, respectively, where the dashed line is the lossless case. In the first picture, we see

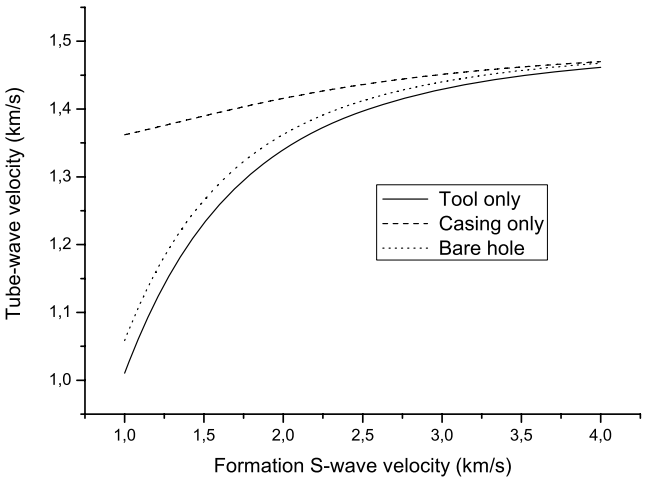


**Figure 4.** Tube-wave velocity as a function of the *S*-wave velocity of the formation. The dotted line represents the case with tool and casing.

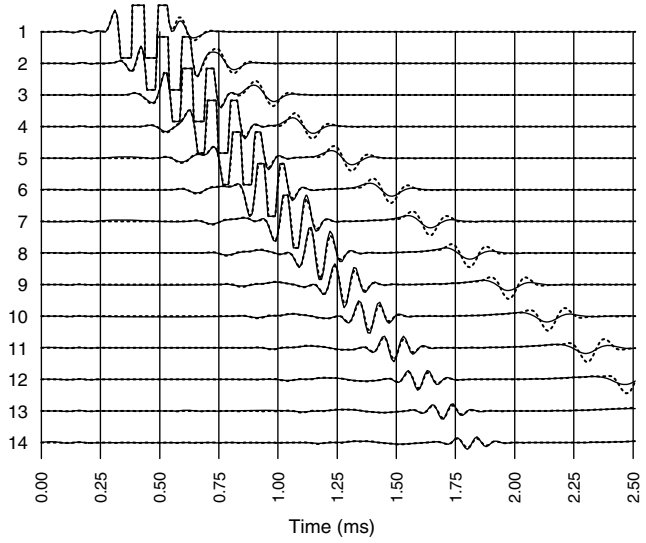


**Figure 5.** $\sigma_{rr}$ waveforms due to a monopole source, corresponding to the soft formation, where the dashed line is the lossless case. The source is an $f_{rr}$ ring of 5.5 cm radius, and the receivers are located at the same radial position. The offset of trace 1 is 40 cm and the distance between traces is 16 cm.

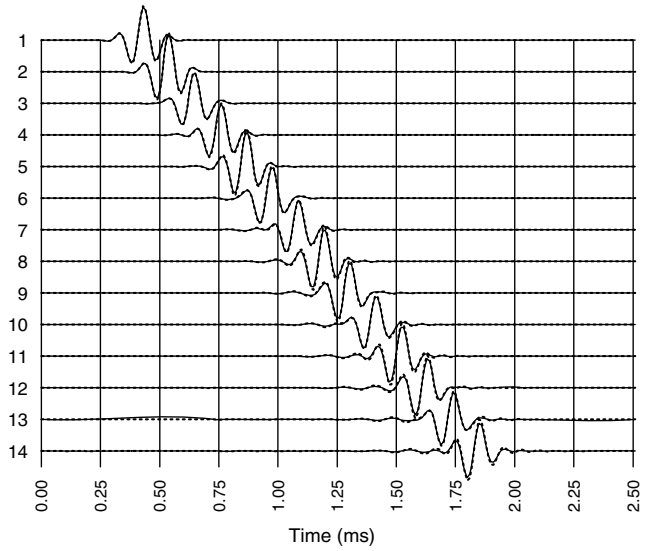


**Figure 6.** $\sigma_{rr}$ waveforms due to a monopole source, corresponding to the hard formation, where the dashed line is the lossless case.

a weak *P* wave arriving first, followed by a water wave and the Stoneley wave. The identification of the latter is based on eq. (49). The distance between traces 1 and 11 is 160 cm. Considering that the traveltime difference between the peaks of the latter event is roughly 1.7 ms, we obtain a velocity of 941 m s$^{-1}$, very close to the one obtained from eq. (49) for a soft formation, that is, 946 m s$^{-1}$. Similarly, the approximate peak differences of the first and second events are 0.64 and 1.05 ms, giving velocities of 2500 and 1520 m s$^{-1}$, corresponding to the *P* waves in the formation and the fluid, respectively. The intrinsic attenuation of the formation affects the Stoneley wave in the soft-formation case. Figs 7 and 8 correspond to the dipole and the quadrupole in a soft formation, respectively. In these cases, according to Chen (1988, 1989), trains of *S* waves are more significant than in the monopole case.

Fig. 9 corresponds to Fig. 5 but including the casing. It resembles that of the hard formation (see Fig. 6), where the water wave is dominant. As found above, the Stoneley velocity for the soft formation with casing is similar to that of the hard formation. The Stoneley wave is much weaker than the water wave.

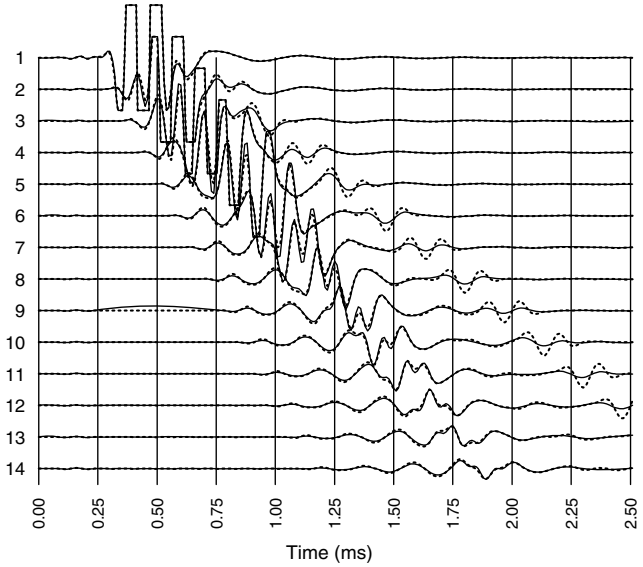


**Figure 7.** $\sigma_{rr}$ waveforms due to a dipole source, corresponding to the soft formation, where the dashed line is the lossless case.

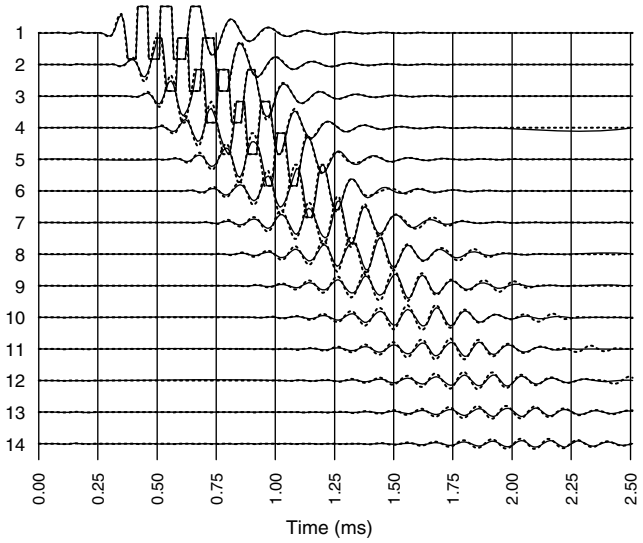


**Figure 8.** $\sigma_{rr}$ waveforms due to a quadrupole source, corresponding to the soft formation, where the dashed line is the lossless case.

Fig. 10 corresponds to Fig. 5, including a layer with a thickness of 56 cm with the properties of the hard formation. The Stoneley wave has disappeared due to the presence of the layer.

The microseismograms are scaled with respect to the maximum amplitude. The relative scales corresponding to Figures, 5–10 are 1, 6, 3, 1, 6 and 1, respectively.

## 7 CONCLUSIONS

We have developed a modelling algorithm for wave simulation due to multipole sources in boreholes in the presence of the logging tool. The spatial derivatives are computed by using the Fourier and Chebyshev methods along the vertical and radial directions, respectively. The media is uniform along the azimuthal direction,

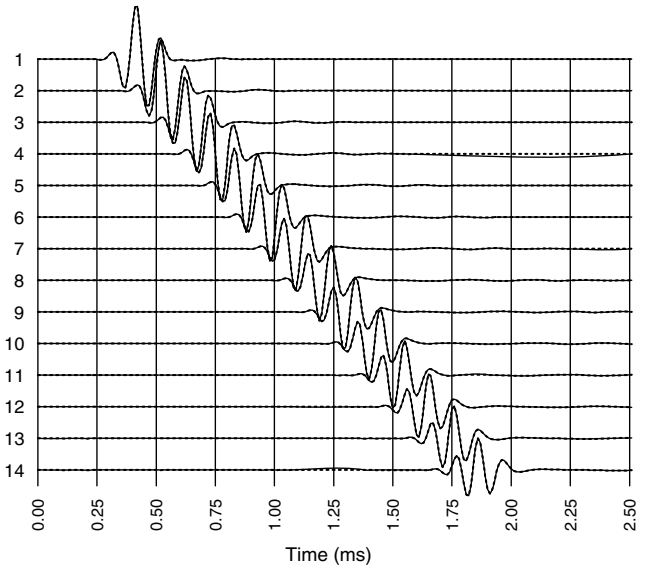


**Figure 9.** $\sigma_{rr}$ waveforms due to a monopole source and a soft formation, in the presence of casing.

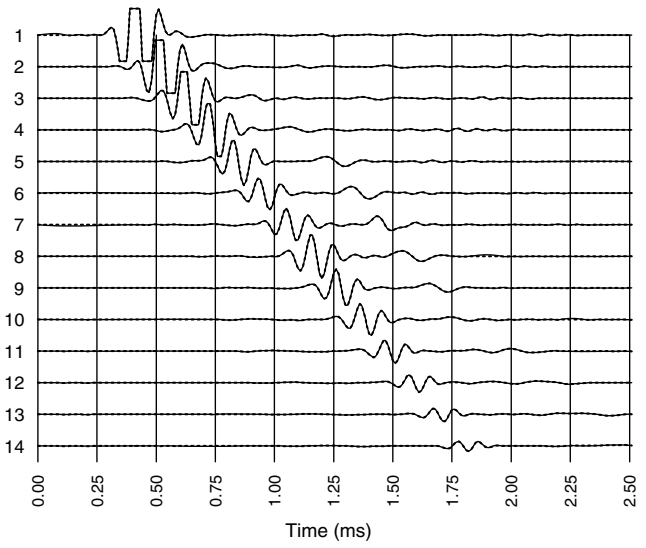


**Figure 10.** $\sigma_{rr}$ waveforms due to a monopole source and a soft formation, in the presence of a high-velocity horizontal layer.

but there are no restrictions along the vertical and radial directions, where any type of inhomogeneity can be modelled. The stress–strain relation is based on the Kelvin–Voigt mechanical model, which describes dissipation involving minimum requirements of computer storage.

We show examples of propagation in hard and soft formations for monopole, dipole and quadrupole sources, including casing and an inhomogeneous formation. The modelling simulates the train of waves involved in acoustic logging, namely, the *P* and *S* waves, the Stoneley wave, and the dispersive *S* waves in the case of dipole and quadrupole sources. The simulations include all the modes observed in real data; the assumed axisymmetry does not pose any limitation in this sense, and it is generally a good approximation for sonic logging.

## ACKNOWLEDGMENTS

We thank two anonymous reviewers for helpful comments.

## REFERENCES

Ben-Menahem, A. & Singh, S.J., 1981. *Seismic Waves and Sources,* Springer-Verlag, New York.

Carcione, J.M., 1991, Domain decomposition for wave propagation problems, *J. Sci. Comput.*, **6,** 453–472.

Carcione, J.M., 1994. Modeling elastic waves in the presence of a borehole and free surface, in *The 64th Ann. Internat. Mtg., Soc. Expl. Geophys.,* Expanded Abstracts.

Carcione, J.M., 1996. A 2-D Chebyshev differential operator for the elastic wave equation, *Comput. Methods Appl. Mech. Engrg.*, **130,** 33–45.

Carcione, J.M., 2007. *Wave Fields in Real Media. Theory and Numerical Simulation of Wave Propagation in Anisotropic, Anelastic, Porous and Electromagnetic Media,* Elsevier, Amsterdam.

Carcione, J.M. & Poletto, F., 2000. Simulation of stress waves in attenuating drill strings, including piezoelectric sources and sensors. *J. acoust. Soc. Am.*, **108,** 53–64.

Carcione, J.M., Poletto, F. & Gei, D., 2004. 3-D wave simulation in anelastic media using the Kelvin–Voigt constitutive equation, *J. Comput. Phys.*, **196,** 282–297.

Chen, S.T., 1982. The full acoustic wave train in a laboratory model of a borehole, *Geophysics*, **47,** 1512–1520.

Chen, S.T., 1988. Shear-wave logging with dipole sources, *Geophysics*, **53,** 659–667.

Chen, S.T., 1989. Shear-wave logging with quadrupole sources, *Geophysics*, **54,** 590–597.

Chen, Y–H., Chew, W.C. & Liu, Q.-H., 1998. A three-dimensional finite difference code for the modeling of sonic logging tools, *J. acoust. Soc. Am.*, **103,** 702–712.

Emmerich, H. & Korn, M., 1987. Incorporation of attenuation into time-domain computations of seismic wave fields, *Geophysics*, **52,** 1252–1264.

Fung, Y.C., 1965. *Foundations of Solid Mechanics,* Prentice-Hall Inc., Engelwood Cliffs, New Jersey.

Kumar, R. & Ram, S., 1969. Flexural vibrations of a fluid-filled cylindrical cavity in an infinite solid medium, *Acustica*, **22,** 163–171.

Kurkjian, A.L. & Chang, S.K., 1986. Acoustic multipole sources in fluid-filled boreholes, *Geophysics*, **61,** 148–163.

Marzetta, T.L. & Schoenberg, M., 1985, Tube waves in cased boreholes, in *The 55th Ann. Int. Mtg., Soc. Expl. Geophys.,* Expanded Abstracts, pp. 34–36.

Mittet, R. & Renlie, L., 1996. High-order, finite-difference modeling of multipole logging in formations with anisotropic attenuation and elasticity. *Geophysics*, **51,** 21–33.

Norris, A.N., 1990. The speed of the tube wave, *J. acoust. Soc. Am.*, **87,** 414–417.

Paillet, F.L. & Cheng, C.H., 1991. *Acoustic Waves in Boreholes,* CRC Press. Inc., New York.

Poletto, F., Carcione, J.M., Lovo, M. & Miranda, F., 2002. Acoustic velocity of SWD borehole guided waves, *Geophysics*, **67,** 921–927.

Randall, C.J., Scheibner, D.J. & Wu, P.T., 1991. Multipole borehole acoustic waveforms: synthetic logs with beds an borehole washouts, *Geophysics*, **56,** 1757–1769.

Tichelaar, B.W. & van Luik, K.W., 1995. Sonic logging of compressional-wave velocities in a very slow formation, *Geophysics*, **60,** 1627–1633.

White, J.E., 1965. *Seismic Waves: Radiation, Transmission and Attenuation,* McGraw Hill.

White, J.E. & Zechman, R.E., 1968. Computed response of an acoustic logging tool, *Geophysics*, **33,** 302–310.

Winbow, G.A., 1985. Compressional and shear arrivals in a multipole sonic log, *Geophysics*, **50,** 1119–1126.

Winbow, G.A., 1991. Seismic sources in open and cased boreholes, *Geophysics*, **56,** 1040–1050.